Power Quality Improvement for Grid-connected PV System Based on Distribution Static Compensator with Fuzzy Logic Controller and UVT/ADALINE-based Least Mean Square Controller

Amit Kumar and Pradeep Kumar

***Abstract*—This paper presents a novel method of power quality enrichment in a grid-connected photovoltaic (PV) system using a distribution static compensator (DSTATCOM). The paper consists of two-step control processes. In the primary step, a fuzzy logic controller (FLC) is employed in the DC-DC converter to extract the peak power point from the PV panel, where the FLC produces a switching signal for the DC-DC converter. In the secondary step, a unit vector template (UVT)/adaptive linear neuron (ADALINE)-based least mean square (LMS) controller is adopted in the DC-AC converter, i.e., voltage source converter (VSC). The input to this VSC is the boosted DC voltage, which originates from the PV panel as a result of DC-DC conversion. The VSC shunted with the power grid is known as a DSTATCOM, which can maintain the power quality in the distribution system. The UVT controller generates reference source currents from the grid voltages and DC-link voltages. The ADALINE-based LMS controller calculates the online weight according to the previous weights by the sensed load current. The UVT/ADALINE-based LMS controller of a DSTATCOM performs several tasks such as maintaining the sinusoidal source current, achieving a unity power factor, and performing reactive power compensation. The reference current extracted from the UVT/ADALINE-based LMS controller is fed to the hysteresis current controller to obtain the desired switching signal for the VSC. A 100 kW solar PV system integrated into a three-phase four-wire distribution system through a four-leg VSC is designed in MATLAB/Simulink. The performances of the FLC and UVT/ADALINE-based LMS controllers are demonstrated under various irradiances as well as constant temperature and nonlinear loading conditions.**

***Index Terms*—Adaptive linear neuron, least mean square (LMS), fuzzy logic controller (FLC), maximum power point tracking (MPPT), photovoltaic (PV), unit vector template.**

I. Introduction

As limited resources exist for conventional energy, the requirement for renewable energy resources is growing exponentially. Demands for renewable power supplies are increasing because of their inherent advantageous characteristics such as the ability to regenerate, constant availability, pollution-free properties, and low maintenance cost after commissioning [1]-[3]. In previous studies, solar photovoltaic (PV) systems are highlighted as the most popular and clean renewable energy resources [1]-[5]. The PV system is considered the most important renewable energy resource globally, with applications in both generation and grid integration [4]. However, the main issues with PV systems are their efficiency, grid integration, quality of uninterrupted power, and grid stability [6], [7].

Many studies have attempted to improve the efficiencies of PV systems and reduce installation costs [1]-[9]. To improve the efficiency of conversion, maximum power point tracking (MPPT) methods have been studied, including perturb and observe (P&O) [6], [10], [11], incremental conductance [10]-[15], fractional open circuit voltage [11], fuzzy-logic-based [16], and artificial-intelligence-based [11], [14] methods. Incremental conductance and P&O are the most commonly used methods because of their simplicity and ease of implementation. However, these methods have drawbacks, including slow convergence, fixed perturbation steps, low efficiency under dynamic conditions, and oscillation around the final point [11]-[14]. The hill-climbing method generates a duty cycle disturbance, resulting in increased oscillation toward the optimal or terminal point [12]. Soft-computing-based algorithms such as particle swarm optimization (PSO), Jaya optimization algorithm, and ant colony optimization (ACO) have recently gained popularity, but their large-population-sized data creates complexity [17]. Among the methods with superior qualities, the fuzzy logic controller (FLC) has exhibited great performance in nonlinear system tuning. FLC is simpler in nature and adapts to changing environments. It does not require prior data and has a faster convergence rate. Some studies have examined the means of increasing the output power and improving PV systems for supplying active power to the power grid, but few have addressed power quality issues such as harmonic elimination, reactive power burden, phase imbalance, and deterioration of power factor. Power converters are the primary means of transferring power from solar PV systems to the power grid

Manuscript received: May 10, 2021; accepted: November 2, 2021. Date of CrossCheck: November 2, 2021. Date of online publication: November 30, 2021.

A. Kumar and P. Kumar (corresponding author) are with the Electrical and Electronics Engineering Department, Natioanl Institute of Technology Sikkim, Sikkim, India (e-mail: phee17003@nitsikkim.ac.in; pradeep@nitsikkim.ac.in).

DOI: 10.35833/MPCE.2021.000285

[5] - [9]. A distribution static compensator (DSTATCOM) is an interfacing device between solar PV systems and the grid and helps mitigate power quality issues arising from nonlinear loads such as computers, adjustable speed drives, and fluorescent lamps [8]. The interfacing of solar PV systems to the grid through a DSTATCOM can critically address power quality issues such as harmonics, reactive power burden, and phase imbalance [8] - [13]. At the consumer side, if a load changes continuously, then the reactive power demand also changes, and the grid power quality in turn fluctuates. Developing a system that continuously monitors power quality and synchronizes the signal with a solar PV system is a major challenge. Several controllers have been employed to improve the characteristics of DSTATCOM, including synchronous reference frame (SRF) theory [8], instantaneous reactive power theory (IRPT) [8], sliding mode controllers [8], power balancing theory (PBT) [8], and second-order generalized integrator (SOGI)-based theory [17], [18]. Low-pass filters (LPFs) and phase-locked loops (PLLs) are major parts of SRF IRPT, unit vector template (UVT) controllers and other traditional controllers. The estimated signals are delayed because of these two blocks. PLLs must also be tuned using the SRF method, but they have the following disadvantages: more time are required to implement in digital circuits; longer computation time; less effective in correcting distortion in voltage profiles; and voltage frequency changes. The design of the sliding surface in a dynamic system represents a major flaw in the sliding-mode control method. If the design of the surface is not adequate, then the performance in dynamic situations deteriorates. Thus, in dynamic situations, this control method is ineffective. The adaptive linear neuron (ADALINE)-based LMS controller is not subject to LPFs, PLLs, and the other limitations of traditional controllers. In this paper, an ADALINE-based LMS or UVT control is used to control the DSTATCOM for obtaining the superior power-quality features of the proposed control. The ADALINE controller has the following advantages. It does not use a PLL [19]; low computational burden [20]; more efficient under dynamic load changes; and high noise-rejection capabilities [5].

The remainder of this paper is organized as follows. Section II describes the grid-connected PV system. Section III elaborates on the theory of DC-DC boost converter. Section IV details the second-stage converter controller. Section V presents the discussion of results. Section VI concludes the paper.

II. Grid-connected PV System

The circuit arrangement of a solar PV panel integrated with a three-phase four-wire grid through DSTATCOM is shown in Fig. 1. Two-stage controllers are utilized in this system, i. e., a step-up DC-DC converter in the first stage and a voltage source DC-AC boost converter in the second stage. The circuit consists of a 100-kW rated PV panel, DC-DC boost converter, voltage source converter (VSC), grid, and various types of loads. The boost converter has one insulated gate bipolar transistor (IGBT)-based switch S0, a filter inductor L_1, a ripple-free absorbing filter C_1, and a diode D_1. I_{pv} and V_{pv} are the output current and voltage of the PV panel, respectively; and C_{dc1} and C_{dc2} are the DC link capacitors that connect the boost converter and VSC for voltage transfer. A four-leg VSC topology is formed by the eight IGBT/diode switches S1-S8 of the DC-AC converter. The interface inductor L_f compensates for the current harmonics of the DC-AC converter; V_{dc} is the voltage of DC-link capacitor; R_s and L_s are the resistance and inductance of the grid, respectively; i_{sa}, i_{sb}, and i_{sc} are the three-phase source currents; i_{sn} is the neutral current of the grid; and i^*_{sa}, i^*_{sb}, and i^*_{sc} are the reference currents generated by the proposed controller.

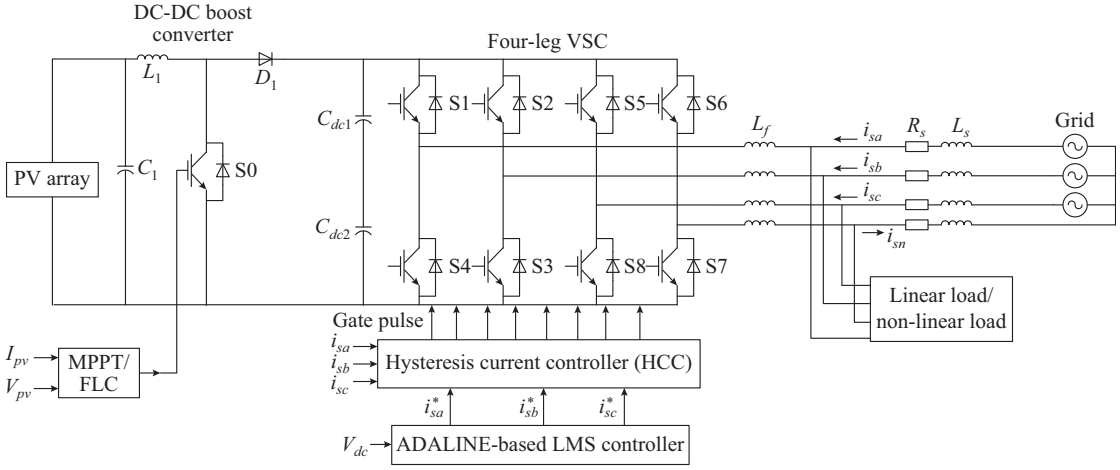

Fig. 1. Structure of a grid-integrated PV panel.

A. Design of PV System

The single-diode PV model in equivalent arrangement is shown in Fig. 2. This single-diode model is intensive for determining the *I-V* and *P-V* characteristics of different PVs based on different parameters associated with each PV. The output current I_{pv} of the PV cell is obtained by relating Kirchhoff's current law:

$$I_{pv} = I_{ph} - I_{diode} - I_r \tag{1}$$

$$I_{pv} = I_{ph} - I_o\left(\mathrm{e}^{\frac{V+IR_s}{a}} - 1\right) - \frac{V+IR_s}{R_p} \tag{2}$$

where I_{diode} is the current through the diode; R_p is the shunt resistance; I_{ph} is the current generated by the PV panel; I_r is the current through the shunt resistance; a is the modified ideality factor; and R_2 is the resistance of the load.

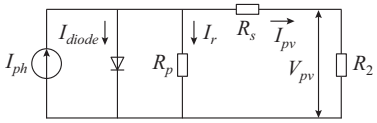

Fig. 2. Single-diode PV model in equivalent arrangement.

Figure 3 shows the *I-V* and *P-V* curves of the PV system with various irradiances at a constant temperature of 25 °C. The standard set of irradiance and constant temperature values can also be found in this figure. Each curve has a certain peak at a different magnitude. This means that as the irradiance output power changes, the PV voltage also changes. When the PV operates at an irradiance of 1 kW/m^2, it generates a maximum output power of 300 W and decreases continuously with a decrease in irradiance. The point at which the PV produces its peak power is called the peak power point, which varies depending on the output voltage. Thus, developing a mechanism that holds the maximum power point of the PV at a standard level under dynamic environmental conditions is essential. This mechanism is called the MPPT.

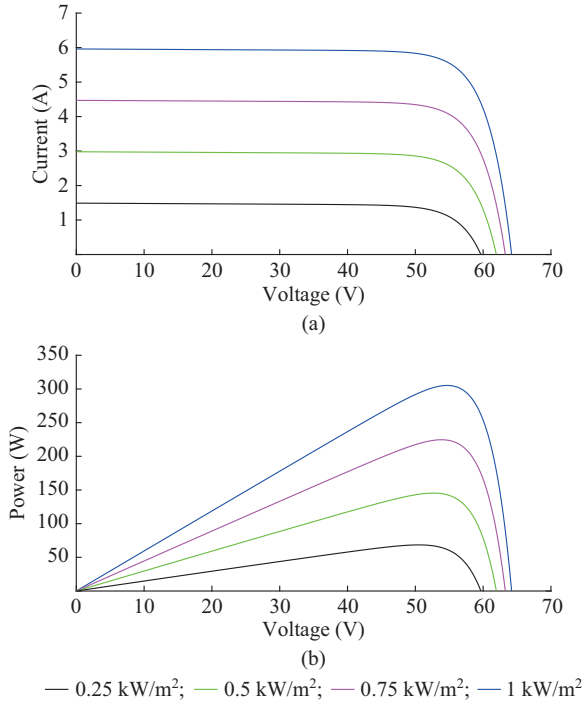

Fig. 3. *I-V* and *P-V* curves of PV system with different irradiances at a constant temperature of 25 °C. (a) *I-V* curve. (a) *P-V* curve.

B. Design of PV Panel

The maximum output power under standard test conditions (STCs) of 1000 W/m^2 is obtained by:

$$P_{mp} = (N_s V_{mp})(N_p I_{mp}) \tag{3}$$

The number of series-connected module is N_s = 66, the voltage at the maximum power under STCs is V_{mp} = 54.7 V, the number of parallel connected modules is N_p = 5, and the current at the maximum power under STCs is I_{mp} = 5.58 A. P_{mp} is (66 × 54.7 V) × (5 × 5.58 A) = 100724.58 W ≈ 100 kW. The specifications of PV panel is shown in Table I.

TABLE I
SPECIFICATIONS OF PV PANEL

Parameter	Value
Per-unit cells	96
Open-circuit voltage V_{oc}	64.2 V
Short-circuit current I_{sc}	5.56 A
Voltage at crest power level V_{mp}	54.7 V
Current at crest power level I_{mp}	5.58 A
Number of modules in a series	66
Number of modules in a parallel	5
The maximum power under STC P_{mp}	100 kW

III. THEORY OF DC-DC BOOST CONVERTER

Figure 4 depicts the schematic of PV panel with an MPPT/FLC controlled boost converter. The boost converter has one switch, a filter inductor L_1, a ripple-free absorbing filter C_1, and a diode D_1. In Fig. 4, D is the duty cycle generated from the MPPT and R_L is the load resistance. The output power of the PV array primarily depends on the array's modular structure and climatic factors such as irradiance and temperature, which affect the generated output power of the PV. The inconsistent power generated by the PV panel makes it unsuitable for grid-connected systems. Therefore, to better utilize output power of the PV, PV panels should operate consistently at their maximum power point voltage.

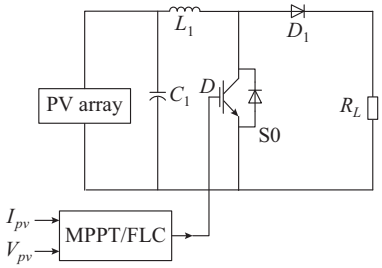

Fig. 4. Schematic of PV panel with an MPPT/FLC controlled boost converter.

In this paper, a DC-DC converter with MPPT is used to optimize the generated output power, allowing the PV panel to be used more efficiently. The first step is to control the duty cycle of the boost converter. The DC voltage of the PV array should be first incrementally increased to a high DC voltage as required by the load. This works on the principle of storing energy in the inductor and transferring it to the load whenever required. This entire process is performed by the gate pulse input, i. e., duty cycle. Therefore, controlling the duty cycle is critical. The next step is to obtain the highest power from the PV array regardless of the environmental conditions and temperature. The two most important parameters for obtaining the maximum power and voltage from a

PV array are the irradiance and temperature. Thus, the highest power level, which is close to the maximum power of the PV array, must be tracked. To construct a standard efficient tracking system, the MPPT has been developed. In previous studies, many MPPT techniques are considered for tracking the highest power. However, some disadvantages have been identified in certain MPPT techniques such as P&O [9], which employs step-size control and oscillates around the steady state under dynamic changing environmental conditions. The incremental conductance [15] algorithm exhibits a high response time in changing environments but has a higher cost and greater complexity. Finally, the constant voltage [10] technique has been found to be less efficient than other MPPT techniques. Therefore, the fuzzy-logic-based MPPT controller is chosen to overcome the step-size problem under dynamic conditions, thereby enabling greater efficiency. This controller has a less response time, is more robust, and can perform tasks in imprecise range of input.

A. FLC

The FLC works on deciding the output based on the assumption. Conventional logic systems are based on only "true and false" values, whereas fuzzy logic uses changing values. Figure 5 shows the flow of an FLC.

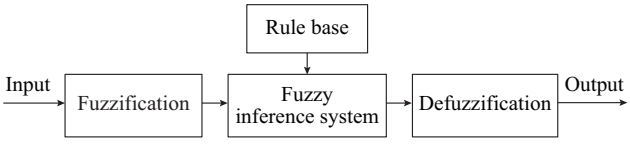

Fig. 5. Flow of an FLC.

B. FLC Execution in MPPT

MPPT in FLC is shown in Fig. 6 for obtaining the duty cycle and tracking the maximum power point, where $P(k)$ is the power at the k^{th} instant; $P(k-1)$ is the power at the $(k-1)^{th}$ instant; $V(k)$ is the voltage at the k^{th} instant; and $V(k-1)$ is the voltage at the $(k-1)^{th}$ instant.

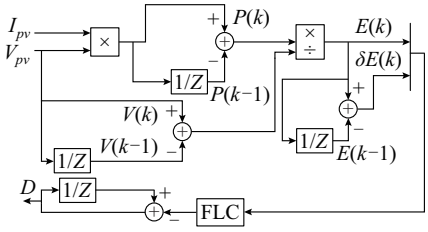

Fig. 6. MPPT in FLC.

Step 1: input modeling.

Two inputs are required to implement the MPPT. The first is the derivative of the PV power dP_{pv} and PV voltage dV_{pv}, which is the error E, and the second is the change in error, i.e., δE.

Input 1:

$$E(k)=dP_{pv}/dV_{pv}=P(k)-P(k-1)/\left(V(k)-V(k-1)\right) \quad (4)$$

Input 2:

$$\delta E(k)=E(k)-E(k-1) \quad (5)$$

Step 2: fuzzification.

After the input from the PV panel is received, the fuzzification is performed using Mamdani's method. This converts input variables into linguistic variables [21], [22]. To achieve this, creating different membership functions for the input and output is necessary. In this paper, five triangular membership functions, i. e., negative big (NB), negative small (NS), zero value (ZE), positive small (PS), and positive big (PB), are in the range of different inputs and outputs. Inputs 1 and 2, and the output ranges of [–10, 10], [–20, 20], and [–2, 2] are shown in Fig. 7.

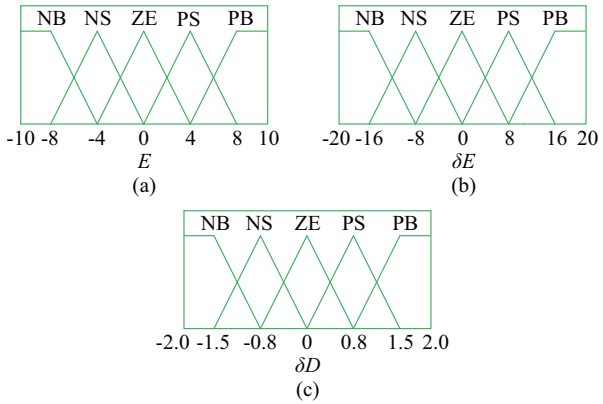

Fig. 7. Fuzzy membership functions for input and output variables. (a) Input 1. (b) Input 2. (c) Output.

Step 3: fuzzy rule setup.

After the input and output membership functions are obtained, a rule is designed and then is applied to the fuzzy inference system. A rule is not designed as earlier logic "true" or "false". Here, "AND" logic gate rule has been implemented for FLC rule setup.

Rule 1: if E is PB "AND" δE is PB, the output will be PB.

Rule 2: if E is PS "AND" δE is PB, the output will be PB.

Rule 25: if E is NB "AND" δE is NB, the output will be NB.

Based on these assumptions, 25 rules are designed, and the "AND" rule is applied to the FLC, as shown in Table II.

TABLE II
FUZZY RULES DESIGNED BASED ON MEMBERSHIP FUNCTIONS

δE	E				
	PB	PS	ZE	NS	NB
PB	PB	PB	PB	PS	ZE
PS	PB	PB	PS	ZE	NS
ZE	PS	PS	ZE	NS	NS
NS	ZE	ZE	NS	NB	NB
NB	NS	NS	NB	NB	NB

Step 4: defuzzification.

In this process, the fuzzified set rule base is converted to a "crisp output" real number. The output value, which is the change in the duty cycle of the boost converter, is fed to the workspace area of MATLAB in real time. The main advan-

tage of the FLC is that it works very quickly in dynamic systems with changing environments and imprecise input.

IV. Second-stage Converter Controller

A. UVT Controller

The structure of UVT controller is illustrated in Fig. 8. This controller creates reference source currents i_{sa}^*, i_{sb}^*, and i_{sc}^* for HCC [18]. The HCC constructs switching signals for the VSC-based DSTATCOM. The following steps are used to generate the reference source currents.

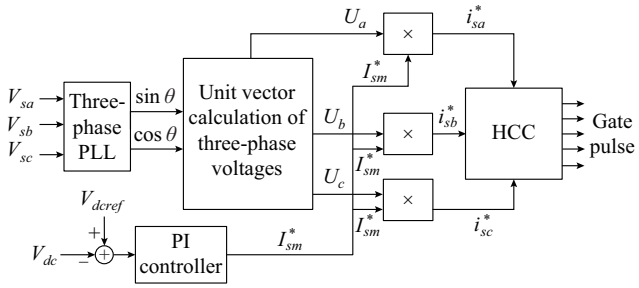

Fig. 8. Structure of UVT controller.

Step 1: three-phase grid voltages V_{sa}, V_{sb}, and V_{sc} are sensed and fed to the three-phase PLL. The PLL creates an output as a unit vector component of $\sin\theta$ and $\cos\theta$.

Step 2: this unit vector component is employed to calculate 120° shifted units $U_a, U_b,$ and U_c.

$$U_a = \sin\omega t \tag{6}$$

$$U_b = \sin(\omega t - 120°) \tag{7}$$

$$U_c = \sin(\omega t + 120°) \tag{8}$$

Step 3: to obtain the peak values of the reference source currents, the proportional-integral (PI) controller processes the DC voltage error i_{sm}^* generated from the difference between the reference DC voltage V_{dcref} and V_{dc}. At the source side, the three-phase reference currents are calculated by multiplying the shifted units and peak value.

$$i_{sa}^* = U_a i_{sm}^* \tag{9}$$

$$i_{sb}^* = U_b i_{sm}^* \tag{10}$$

$$i_{sc}^* = U_c i_{sm}^* \tag{11}$$

Step 4: the HCC employs the reference source currents i_{sa}^*, i_{sb}^*, and i_{sc}^* to generate the desired gate pulse for the VSC-based DSTATCOM.

B. ADALINE-based LMS Controller

After the DC-DC boost converter is controlled, the next task is to control the DC-AC converter or DSTATCOM. An ADALINE-based LMS controller is employed to control the DSTATCOM. The ADALINE-based LMS controller operates based on the training of the load current through a neural network. This means that at every sample time, it gives a new weight, and in the next sample, this weight is then assigned a new weight. This process continues until all samples have been trained. The step-by-step process for achieving the reference source currents is given as follows.

Step 1: the calculation of $Z_L(k)$, which is a part of the *d*-axis component.

Figure 9(a) shows the calculation of $Z_L(k)$, where $V_{dce}(k)$ is the DC voltage error.

$$V_{dce}(k) = V_{dcref}(k) - V_{dc}(k) \tag{12}$$

$$Z_L(k) = Z_L(k-1) + k_{pd}\left(V_{dce}(k) - V_{dce}(k-1)\right) + k_{id}V_{dce}(k) \tag{13}$$

where k_{pd} and k_{id} are the proportional and integral gains of the DC voltage controller, respectively.

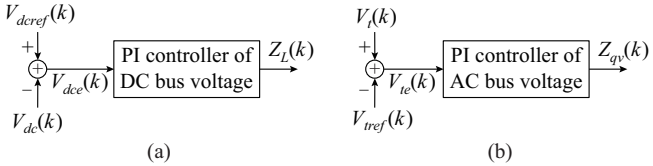

Fig. 9. Calculation of $Z_L(k)$ and $Z_{qv}(k)$. (a) $Z_L(k)$. (b) $Z_{qv}(k)$.

Step 2: the calculation of $Z_{qv}(k)$, which is the part of the *q*-axis component.

Figure 9(b) shows the calculation of $Z_{qv}(k)$, where $V_t(k)$ is the terminal voltage and $V_{tref}(k)$ is the terminal reference voltage.

AC voltage error $V_{te}(k)$ at the k^{th} time is written as:

$$V_{te}(k) = V_t(k) - V_{tref}(k) \tag{14}$$

$$Z_{qv}(k) = Z_{qv}(k-1) + k_{pa}\left(V_{te}(k) - V_{te}(k-1) + k_{ia}V_{te}(k)\right) \tag{15}$$

where k_{pa} and k_{ia} are the proportional and integral constants of the AC voltage controller, respectively.

Step 3: the calculation of weight of the *d*-axis part of the three-phase load currents.

Figure 10(a) shows the calculation of Z_p. The weight of the fundamental *d*-axis component I_d utilizes the LMS control strategy, where the ADALINE neural network is employed for training purposes.

$$Z_{ap}(k) = \left[Z_{ap}(k-1) + \epsilon(I_{La}(k) - Z_{ap}(k-1)U_{ap})\right]U_{ap}(k) \tag{16}$$

$$Z_{bp}(k) = \left[Z_{bp}(k-1) + \epsilon(I_{Lb}(k) - Z_{bp}(k-1)U_{bp})\right]U_{bp}(k) \tag{17}$$

$$Z_{cp}(k) = \left[Z_{cp}(k-1) + \epsilon(I_{Lc}(k) - Z_{cp}(k-1)U_{cp})\right]U_{cp}(k) \tag{18}$$

where $Z_{ap}(k)$, $Z_{bp}(k)$, and $Z_{cp}(k)$ are the weights of the active power constituent of the fundamental *d*-axis currents of the three phases, respectively; ϵ (=0.01) is the convergence factor; $I_{La}(k)$, $I_{Lb}(k)$, and $I_{Lc}(k)$ are the three-phase load currents; and $U_{ap}(k)$, $U_{bp}(k)$, and $U_{cp}(k)$ are the unit sets of the *d*-axis component of the three-phase voltages. Thus, the average weight of the fundamental *d*-axis component $Z_p(k)$ is:

$$Z_p(k) = \left(Z_{ap}(k) + Z_{bp}(k) + Z_{cp}(k) + Z_L(k)\right)/3 \tag{19}$$

The fundamental reference supply currents I_{sap}^*, I_{sbp}^*, and I_{scp}^* are given by:

$$\begin{cases} I_{sap}^* = Z_p U_{ap} \\ I_{sbp}^* = Z_p U_{bp} \\ I_{scp}^* = Z_p U_{cp} \end{cases} \tag{20}$$

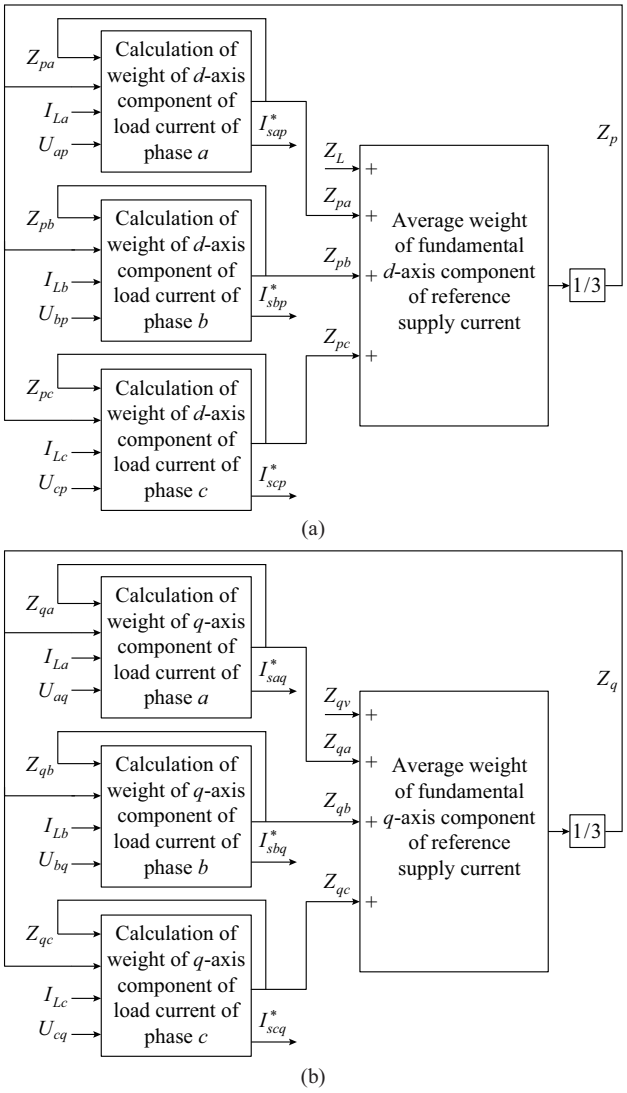

Fig. 10. Calculation of Z_p and Z_q. (a) Z_p. (b) Z_q.

Step 4: the calculation of the weight of q-axis part of the three-phase load currents.

Figure 10(b) shows the calculation of Z_q. The reactive power constituents of the load current and reference supply current are calculated using the following weights.

$$Z_{aq}(k)=\left[Z_{aq}(k-1)+\epsilon(I_{La}(k)-Z_{aq}(k-1)U_{aq})\right]U_{aq}(k) \quad (21)$$

$$Z_{bq}(k)=\left[Z_{bq}(k-1)+\epsilon(I_{Lb}(k)-Z_{bq}(k-1)U_{bq})\right]U_{bq}(k) \quad (22)$$

$$Z_{cq}(k)=\left[Z_{cq}(k-1)+\epsilon(I_{Lc}(k)-Z_{cq}(k-1)U_{cq})\right]U_{cq}(k) \quad (23)$$

where Z_{aq}, Z_{bq}, and Z_{cq} are the weights of the reactive power constituent of the fundamental q-axis current of the three phases. Thus, the average weight of the reference reactive power constituent of the supply current Z_q is:

$$Z_q(k)=\left[Z_{qv}(k)-\left(Z_{qa}(k)+Z_{qb}(k)+Z_{qc}(k)\right)\right]/3 \quad (24)$$

where $Z_{qv}(k)$ is the output of the AC voltage controller.

The fundamental reference q-axis supply currents I^*_{saq}, I^*_{sbq}, and I^*_{scq} are given by:

$$\begin{cases} I^*_{saq}=Z_qU_{aq} \\ I^*_{sbq}=Z_qU_{bq} \\ I^*_{scq}=Z_qU_{cq} \end{cases} \quad (25)$$

Step 5: the generation of signals with pulse width modulation (PWM).

The three-phase reference supply currents from Fig. 11 are given as follows. The calculated reference supply currents $(I^*_{sa}, I^*_{sb}, I^*_{sc})$ are compared with the sensed supply currents (I_{sa}, I_{sb}, I_{sc}) to obtain the current error. The current error provides gating pulses for DSTATCOM switches.

$$I^*_{sa}=I^*_{sap}+I^*_{saq} \quad (26)$$

$$I^*_{sb}=I^*_{sbp}+I^*_{sbq} \quad (27)$$

$$I^*_{sc}=I^*_{scp}+I^*_{scq} \quad (28)$$

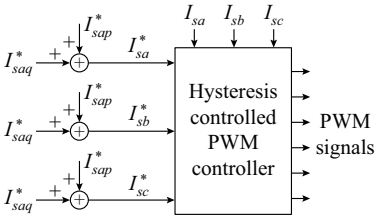

Fig. 11. Generation of PWM signals.

V. Discussion of Results

The performance of each controller in the grid-connected PV system is described in detail as follows.

A. Grid-connected PV System Performance Using UVT Controller

The grid voltage and current waveforms for various solar irradiances are shown in Fig. 12. At every instance of irradiance, both voltage and current are in phase, indicating that the power factor is improving in the presence of an unbalanced nonlinear load. The voltage and current are in phase under a dynamic environment such as when the irradiance changes in periods of 0.7, 1.2, and 1.5 s. This demonstrates the power factor enhancement capabilities of the FLC and UVT controllers in the context of unbalanced nonlinear loads.

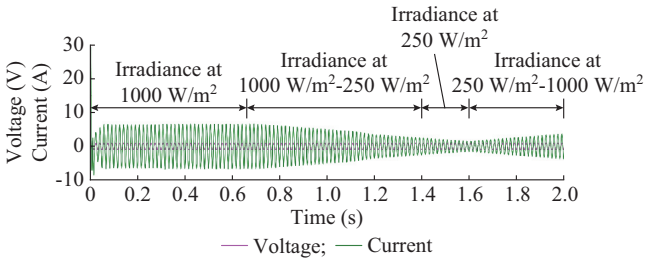

Fig. 12. Grid voltage and current waveforms for various solar irradiances.

Figure 13 demonstrates the DC voltage regulation waveform at time of 0-3 s. The figure shows that after the transient period of 0.21 s, the waveform is stabilized. It is clear from the waveform that the DC bus voltage approaches 500 V and is nearly stabilized at 496 V. The DC bus voltage also changes slightly when the irradiance changes. Figure 14

shows the performances of PV parameters at different solar irradiances. The figure reveals that V_{pv}, which is also the open-circuit voltage of the PV panel V_{oc}, remains nearly constant throughout the simulation. I_{pv} changes continuously when the irradiance changes. At 0-0.7 s, 0.7-1.2 s, 1.2-1.5 s, and 1.5-2.0 s, the irradiances are 1000 W/m^2, 1000 W/m^2-250 W/m^2, and 250 W/m^2, and increase from 250 W/m^2 to 1000 W/m^2, respectively. The performances of DSTATCOM at different solar irradiances are shown in Fig. 15.

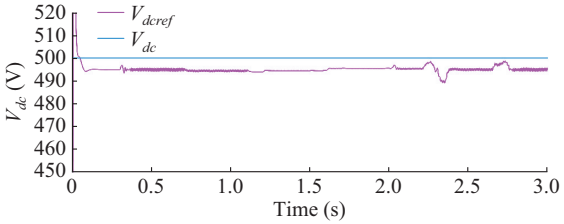

Fig. 13. DC voltage regulation.

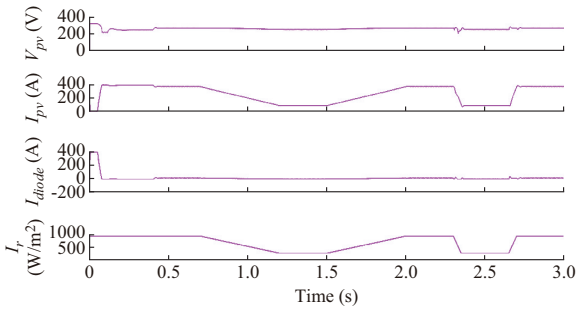

Fig. 14. Performances of PV parameters at different solar irradiances.

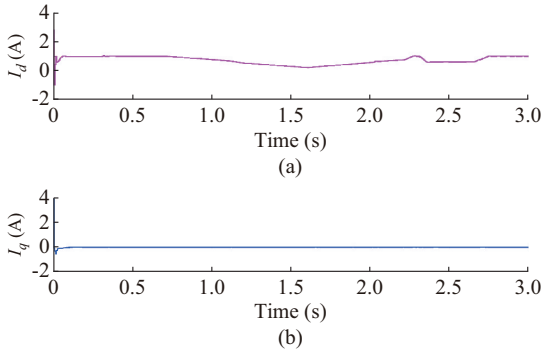

Fig. 15. Performances of DSTATCOM at different solar irradiances. (a) *d*-axis current. (b) *q*-axis current.

The *d*-axis current changes continuously under the environmental condition, i.e., irradiance, as shown in Fig. 15(a). However, the *q*-axis current does not change under environmental conditions. Its magnitude remains zero throughout the period and is unaffected by the irradiance. This shows how the DSTATCOM compensates for the reactive power under dynamic situations. Figure 16 shows the performances of DSTATCOM. The waveform of V_{grid} is sinusoidal throughout the period, and the grid current is sinusoidal but with notches at regular intervals. Figure 17 depicts the total harmonic distortion (THD) of the grid current of the DSTATCOM is in both the off and on modes. The THD should be less than 5% according to the THD specification of the IEEE 519-bus system. The off and on modes result in 34.84% and 3.01% THD of the grid current, respectively.

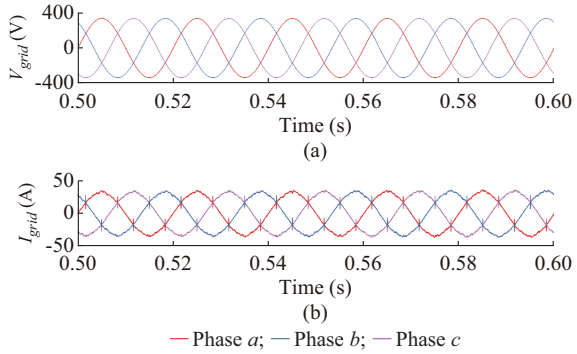

Fig. 16. Performances of DSTATCOM. (a) V_{grid}. (b) I_{grid}.

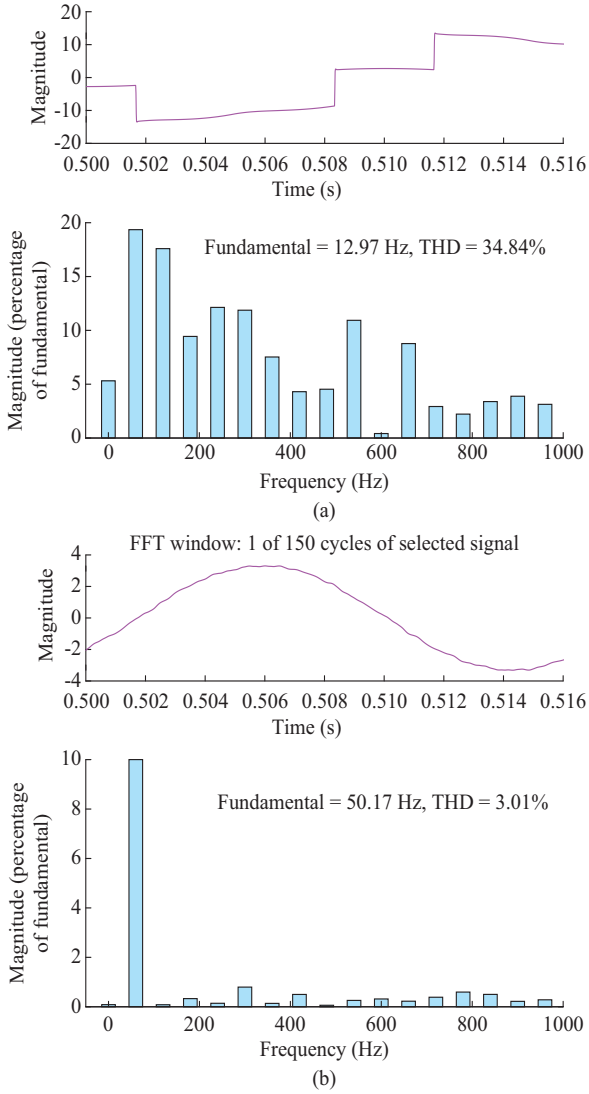

Fig. 17. THD of grid current when DSTATCOM is in off and on modes. (a) DSTATCOM is in off mode. (b) DSTATCOM is in on mode.

B. Performance of Grid-connected PV System with ADALINE-based LMS Controller

The grid voltage and current waveforms at different solar-irradiances are shown in Fig. 18. The voltage and current

waveforms are in the same phase for 0-0.7 s at an irradiance of 1000 W/m^2, indicating that the power factor is unity. At 0.7-1.2 s with an irradiance of 1000 W/m^2-250 W/m^2, the magnitude of the current decreases but is in phase with the voltage. This shows that the performance of DSTATCOM with the ADALINE-based LMS controller works properly under dynamic environmental conditions. Again, at time 1.5-2 s, when the irradiance increases from 250 W/m^2 to 1000 W/m^2, the voltage and current waveforms remain in the same phase. These results thus validate the dynamic performance of the FLC and the ADALINE-based LMS controller of DSTATCOM.

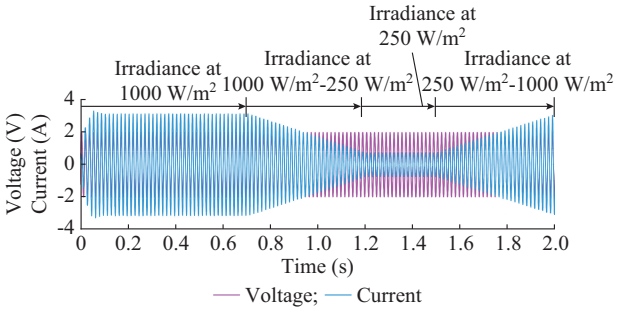

Fig. 18. Grid voltage and current waveforms at different solar irradiances.

Figure 19 shows the performance of the PV parameters V_{pv}, I_{pv}, I_{diode}, and I_r at different irradiances. The figure shows that V_{pv} is nearly constant throughout the simulation period. I_{pv} changes continuously when the irradiance changes. In the aforementioned simulation, the irradiance is 1000 W/m^2 at 0-0.7 s, 1000 W/m^2-250 W/m^2 at 0.7-1.2 s, and 250 W/m^2 at 1.2-2 s. At 1.5-2 s, the value of the irradiance increases to 1000 W/m^2. Figure 20(a) shows the waveform of the q-axis current of the grid. At the transient time, the figure shows a "0" value, which means no reactive power is drawn from the source. Figure 20(b) shows the d-axis current waveform of the grid. Here, the d-axis grid current provides active power. This demonstrates that when the irradiance varies, the direct-axis current changes. The primary reason for this is that the grid provides only active but not reactive power.

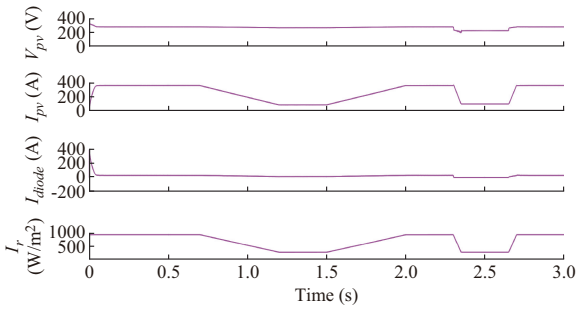

Fig. 19. Performances of PV parameters V_{pv}, I_{pv}, I_{diode}, and I_r at different solar irradiances.

Figure 21 shows the performances of V_{grid} and I_{grid} of the DSTATCOM. The voltage and current are sinusoidal throughout the dynamic scenario. In addition, the effect of the nonlinear load is negligible due to the efficacy of the ADALINE controller.

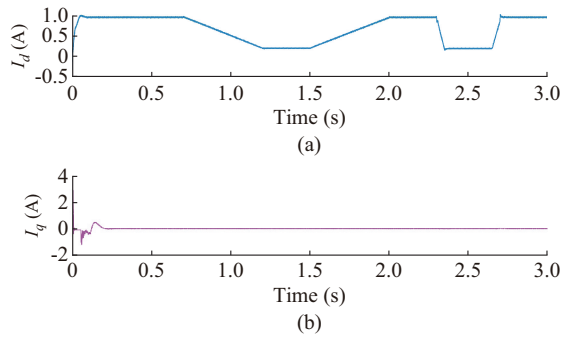

Fig. 20. Performances of DSTATCOM at different solar irradiances with DC and AC voltage regulators. (a) d-axis current (DC voltage regulator). (b) q-axis current (AC voltage regulator).

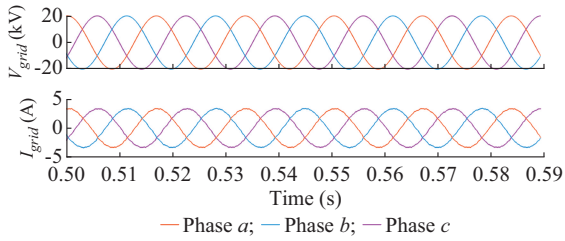

Fig. 21. Performances of V_{grid} and I_{grid} of DSTATCOM.

The DC voltage regulation capabilities of ADALINE controlled DSTATCOM are shown in Fig. 22. The voltage is regulated at 500 V after the transient phase.

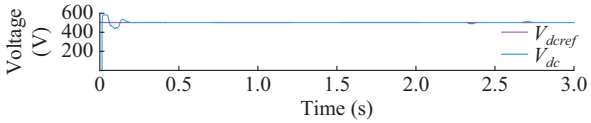

Fig. 22. DC voltage regulation capabilities of ADALINE controlled DSTATCOM.

C. Performance Comparison of UVT and ADALINE-based LMS Controllers

The reactive power compensations with UVT controller and ADALINE-based LMS controller are illustrated in Fig. 23.

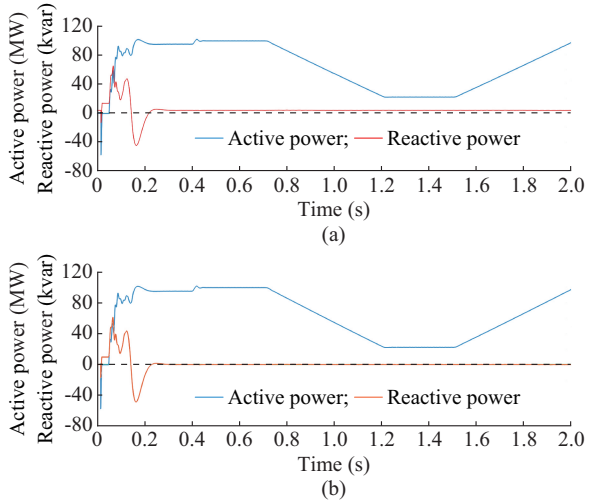

Fig. 23. Reactive power compensation with UVT controller and ADALINE-based LMS controller. (a) UVT controller. (b) ADALINE-based LMS controller.

The reactive power compensation with the UVT controller tends toward but is not exactly zero, which shows that the power factor is leading but does not achieve the unity. By contrast, the reactive power compensation with the ADALINE-based LMS controller is zero after the transient time and remains as shown in the figure. Figure 24 shows that the ADALINE-based LMS controller achieves adequate DC voltage regulation. With the ADALINE-based LMS controller, the grid current waveform is fully sinusoidal and has fewer harmonics, whereas with the UVT controller, the grid current has notches and more harmonics, as shown in Fig. 25.

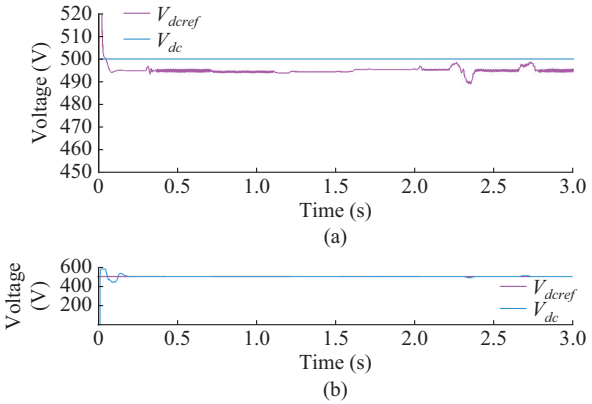

Fig. 24. DC voltage regulation with different controllers. (a) UVT controller. (b) ADALINE-based LMS controller.

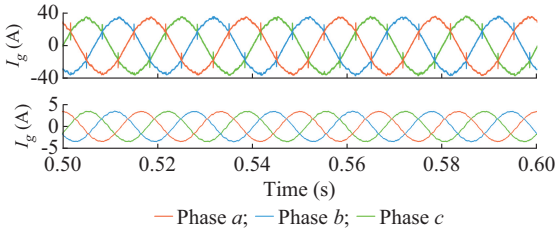

Fig. 25. Grid current with different controllers. (a) UVT controller. (b) ADALINE-based LMS controller.

The estimated frequencies of UVT and ADALINE-based LMS controllers are shown in Fig. 26, which are 0.25 s and 0.18 s, respectively. In addition, Fig. 27 shows that, compared with the UVT controller, the ADALINE-based LMS controller has a lower THD of grid current of 1.94%.

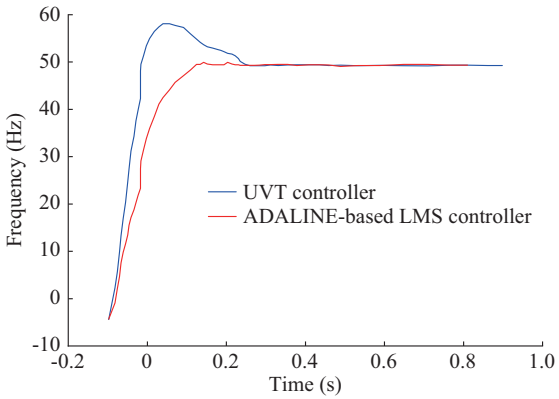

Fig. 26. Estimated frequencies of UVT and ADALINE-based LMS controllers.

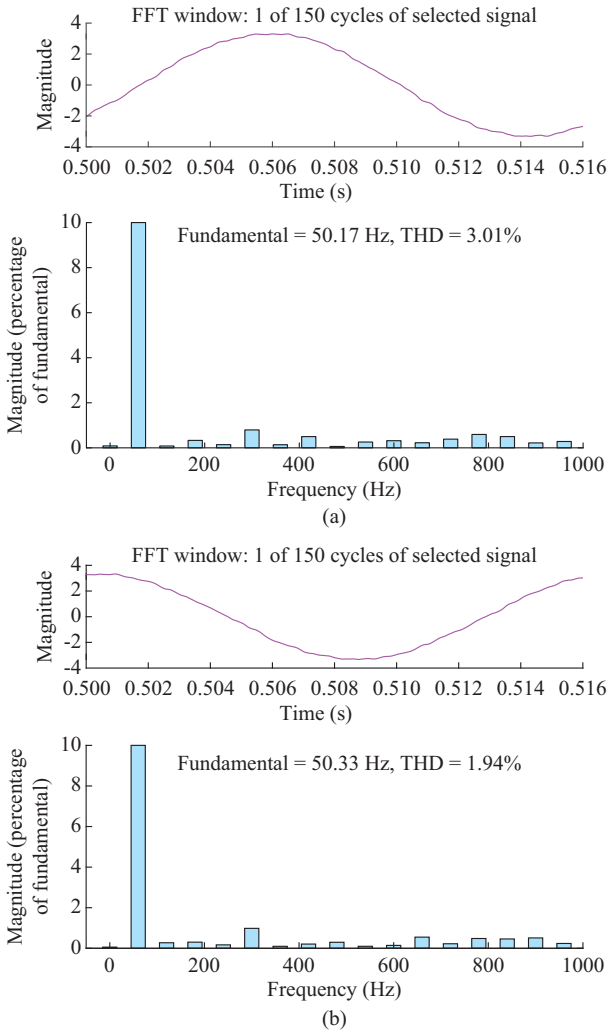

Fig. 27. THD of grid current with different controllers. (a) UVT controller. (b) ADALINE-based LMS controller.

D. Performance Comparison of FLC-based and Conventional MPPTs

Figure 28 presents the comparison of FLC-based and conventional MPPTs in terms of output PV power. The conventional MPPTs include the incremental conductance and the conventional and modified P&O methods.

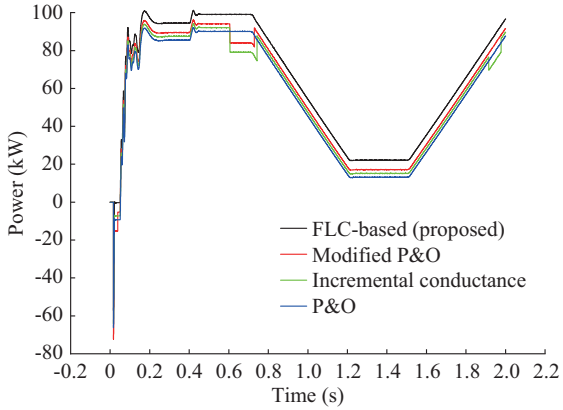

Fig. 28. Comparison of FLC-based and conventional MPPTs in terms of output PV power.

The maximum PV power generated by the PV in the FLC is 96.57 kW, which is approximately identical to the maximum power generated by the PV at an irradiance of 1000 W/m^2 and the constant temperature of 25 ℃. By contrast, the conventional MPPTs produce PV power of less than 96.57 kW under the same conditions.

A comparison of the theoretical performances of the UVT and ADALINE-based LMS controllers is provided in Table III. Figure 29 shows that the ADALINE-based LMS controller performs better than the UVT controller in terms of DC voltage regulation, THD, power factor, and transient time. The values of DC voltage regulation with the UVT and ADALINE-based LMS controllers are 4.95 V and 5 V, respectively. The DC voltage regulations of 495 V and 500 V are taken as 4.95 V and 5 V, respectively, on a 10-point scale.

TABLE III
COMPARISON OF UVT AND ADALINE-BASED LMS CONTROLLERS

Controller	PLL	Computational time	Reference current extraction	Noise rejection capability	Operation method	Real-time execution
UVT	Required	Medium	Slow in dynamic load changing	Poor	No training is required. Only sense the voltages	Less performance
ADALINE-based LMS	Not required	Fast	Fast in dynamic load changing system	Good	Online training is required for extraction of weight	More performance than conventional type controller

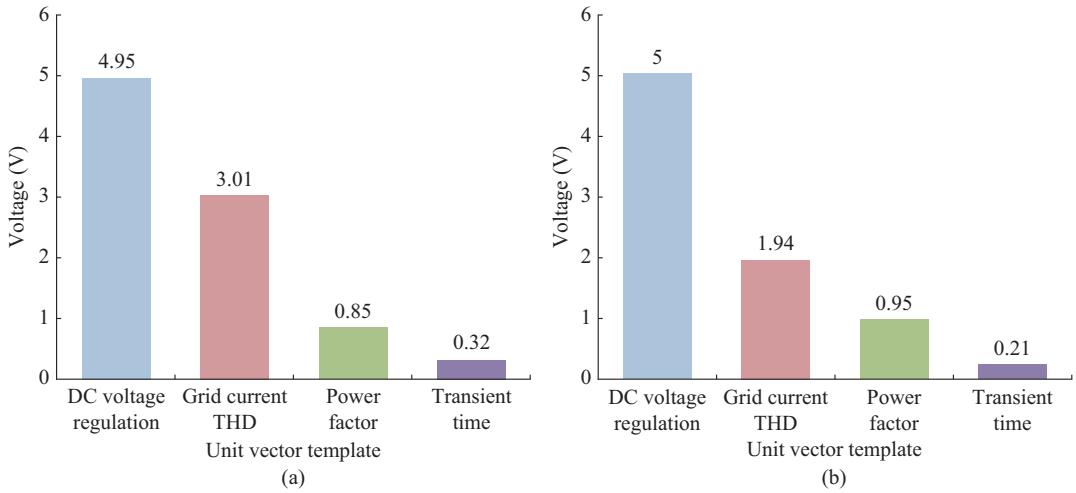

Fig. 29. Performance comparison between UVT and ADALINE-based LMS controllers. (a) UVT controller. (b) ADALINE-based LMS controller.

VI. CONCLUSION

This work proposes a three-phase four-wire grid-integrated PV system that uses a DSTATCOM to address the power quality challenges posed by nonlinear loads. A FLC-based MPPT controller has been executed to track the peak power point. The results show that the FLC-based MPPT controller is more dynamic in varied environments and is less reliant on the input. To extract the maximum power from a PV system, the FLC-based MPPT controller is shown to work well. In addition, an ADALINE-based LMS controller is proposed for the DSTATCOM system. Compared with the UVT controller, the ADALINE-based LMS controller shows improved functionality in mitigating power quality problems caused by nonlinear loads.

REFERENCES

[1] B. Singh, M. Kandpal, and I. Hussain, "Control of grid tied smart PV-DSTATCOM system using an adaptive technique," *IEEE Transactions on Smart Grid*, vol. 9, no. 5, pp. 3986-3993, Sept. 2018.
[2] B. Singh, D. T. Shahani, and A. K. Verma, "Neural network controlled grid interfaced solar photovoltaic power generation," *IET Power Electronics*, vol. 7, no. 3, pp. 614-626, Mar. 2014.
[3] F. Blaabjerg, Z. Chen, and S. B. Kjaer, "Power electronics as efficient interface in dispersed power generation systems," *IEEE Transactions on Power Electronics*, vol. 19, no. 5, pp. 1184-1194, Sept. 2004.
[4] Z. Zou, Z. Wang, and M. Cheng, "Modeling, analysis, and design of multifunction grid-interfaced inverters with output LCL filter," *IEEE Transactions on Power Electronics*, vol. 29, no. 7, pp. 3830-3839, Jul. 2014.
[5] A. K. Singh, I. Hussain, and B. Singh, "Double-stage three-phase grid-integrated solar PV system with fast zero attracting normalized least mean fourth based adaptive control," *IEEE Transactions on Industrial Electronics*, vol. 65, no. 5, pp. 3921-3931, May 2018.
[6] A. K. Abdelsalam, A. M. Massoud, S. Ahmed *et al*., "High-performance adaptive perturb and observe MPPT technique for photovoltaic-based microgrids," *IEEE Transactions on Power Electronics*, vol. 26, no. 4, pp. 1010-1021, Apr. 2011.
[7] R. K. Agarwal, I. Hussain, and B. Singh, "LMF-based control algorithm for single stage three-phase grid integrated solar PV system," *IEEE Transactions on Sustainable Energy*, vol. 7, no. 4, pp. 1379-1387, Oct. 2016.
[8] B. Singh, A. Chandra, and K. AL-Haddad. *Power Quality: Problems and Mitigation Techniques*. Chichester, U.K.: Wiley, 2015.
[9] R. Haider, C. H. Kim, T. Ghanbari *et al*., "Harmonic-signature-based islanding detection in grid-connected distributed generation systems using Kalman filter," *IET Renewable Power Generation*, vol. 12, no. 15, pp. 1813-1822, Nov. 2018.
[10] B. Subudhi and R. Pradhan, "A comparative study on maximum power point tracking techniques for photovoltaic power systems," *IEEE Transactions on Sustainable Energy*, vol. 4, no. 1, pp. 89-98, Jan. 2013.
[11] A. K. Podder, N. K. Roy, and H. R. Pota, "MPPT methods for solar PV systems: a critical review based on tracking nature," *IET Renew-*

able Power Generation, vol. 13, no. 10, pp. 1615-1632, Jul. 2019.
[12] Y. Wang, B. Ren, and Q. Zhong, "Robust power flow control of grid-connected inverters," *IEEE Transactions on Industrial Electronics*, vol. 63, no. 11, pp. 6887-6897, Nov. 2016.
[13] M. A. Elgendy, B. Zahawi, and D. J. Atkinson, "Assessment of the incremental conductance maximum power point tracking algorithm," *IEEE Transactions on Sustainable Energy*, vol. 4, no. 1, pp. 108-117, Jan. 2013.
[14] L. P. Sampaio, M. V. da Rocha, S. A. O. da Silva *et al*., "Comparative analysis of MPPT algorithms bio-inspired by grey wolves employing a feed-forward control loop in a three-phase grid-connected photovoltaic system," *IET Renewable Power Generation*, vol. 13, no. 8, pp. 1379-1390, Jun. 2019.
[15] N. Kumar, I. Hussain, B. Singh *et al*., "Self-adaptive incremental conductance algorithm for swift and ripple-free maximum power harvesting from PV array," *IEEE Transactions on Industrial Informatics*, vol. 14, no. 5, pp. 2031-2041, May 2018.
[16] M. Fannakh, M. L. Elhafyani, and S. Zouggar, "Hardware implementation of the fuzzy logic MPPT in an Arduino card using a Simulink support package for PV application," *IET Renewable Power Generation*, vol. 13, no. 3, pp. 510-518, Feb. 2019.
[17] C. M. Hackl and M. Landerer, "Modified second-order generalized integrators with modified frequency locked loop for fast harmonics estimation of distorted single-phase signals," *IEEE Transactions on Power Electronics*, vol. 35, no. 3, pp. 3298-3309, Mar. 2020.
[18] S. Poongothai and S. Srinath, "Power quality enhancement in solar power with grid connected system using UPQC," *Microprocessors and Microsystems*, vol. 79, no. 8, p. 103300, Nov. 2020.
[19] M. Sujith and S. Padma, "Optimization of harmonics with active power filter based on ADALINE neural network," *Microprocessors and Microsystems*, vol. 73, no. 3, p. 102976, Mar. 2020.
[20] Y. Han, L. Xu, M. M. Khan *et al*., "Robust deadbeat control scheme for a hybrid APF with resetting filter and ADALINE-based harmonic estimation algorithm," *IEEE Transactions on Industrial Electronics*, vol. 58, no. 9, pp. 3893-3904, Sept. 2011.
[21] M. A. A. M. Zainuri, M. A. M. Radzi, A. C. Soh *et al*., "DC-link capacitor voltage control for single-phase shunt active power filter with step size error cancellation in self-charging algorithm," *IET Power Electronics*, vol. 9, no. 2, pp. 323-335, Feb. 2016.
[22] S. Padmanaban, N. Priyadarshi, J. B. Holm-Nielsen *et al*., "A novel modified Sine-Cosine optimized MPPT algorithm for grid integrated PV system under real operating conditions," *IEEE Access*, vol. 7, pp. 10467-10477, Jan. 2019.

Amit Kumar received the B. Tech. degree in electrical engineering from DR. B. C. Roy Engineering College Durgapur, Durgapur, India, in 2010 and the M.Tech. degree in electrical engineering from Birsa Institute of Technology Sindri, Sindri, India, in 2014. He is currently pursuing the Ph.D. degree in electrical and electronic engineering in Natioanl Institute of Technology Sikkim, Sikkim, India. His research interests include power quality, grid synchronization, power electronics converter, and renewable energy systems.

Pradeep Kumar received the B. E. degree in electrical engineering from Government Engineering College Bilaspur, Bilaspur, India, in 2008, the M. Tech. degree in electrical engineering in 2010, and Ph. D. degree in electrical and electronic engineering in 2017 from College of Engineering Pune, Pune, India, and Natioanl Institute of Technology Jamshedpur, Jamshedpur, India, respectively. He is currently working as an Assistant Professor in the Electrical and Electronic Engineering Department, National Institute of Technology Sikkim, Sikkim, India. His research interests include control systems, renewable energy systems, and power quality.